Deep Convective Transition Characteristics in the Community Climate System Model and Changes under Global Warming

SANDEEP SAHANY, J. DAVID NEELIN, AND KATRINA HALES

Department of Atmospheric and Oceanic Sciences, University of California, Los Angeles, Los Angeles, California

RICHARD B. NEALE

National Center for Atmospheric Research, Boulder, Colorado

(Manuscript received 3 December 2013, in final form 25 September 2014)

ABSTRACT

Tropical deep convective transition characteristics, including precipitation pickup, occurrence probability, and distribution tails related to extreme events, are analyzed using uncoupled and coupled versions of the Community Climate System Model (CCSM) under present-day and global warming conditions. Atmospheric Model Intercomparison Project–type simulations using a 0.5° version of the uncoupled model yield good matches to satellite retrievals for convective transition properties analyzed as a function of bulk measures of water vapor and tropospheric temperature. Present-day simulations with the 1.0° coupled model show transition behavior not very different from that seen in the higher-resolution uncoupled version. Frequency of occurrence of column water vapor (CWV) for precipitating points shows reasonable agreement with the retrievals, including the longer-than-Gaussian tails of the distributions. The probability density functions of precipitating grid points collapse toward similar form when normalized by the critical CWV for convective onset in both historical and global warming cases. Under global warming conditions, the following statements can be made regarding the precipitation statistics in the simulation: (i) as the rainfall pickup shifts to higher CWV with warmer temperatures, the critical CWV for the current climate is a good predictor for the same quantity under global warming with the shift given by straightforward conditional instability considerations; (ii) to a first approximation, the probability distributions shift accordingly, except that (iii) frequency of occurrence in the longer-than-Gaussian tail increases considerably, with implications for occurrences of extreme events; and, thus, (iv) precipitation conditional averages on CWV and tropospheric temperature tend to extend to higher values.

1. Introduction

It is challenging for coupled global climate models to produce realistic simulations of precipitation regional patterns, temporal variations, and statistics such as frequency and intensity of rainfall (e.g., Covey et al. 2003; Trenberth et al. 2003; Meehl et al. 2005). Many climate models still leave much to be desired in simulating realistic precipitation statistics, although considerable progress is being made. Energy balance places constraints on the global-mean rainfall, but spatiotemporal patterns have more subtle constraints and hence can be difficult to model. Occurrence probability of precipitation is one major characteristic of rainfall that climate models have struggled to capture. Many weather and climate models tend to precipitate too frequently at low intensities, even when the simulated mean values are reasonable (Chen et al. 1996; Osborn and Hulme 1998; Dai et al. 1999; Trenberth et al. 2003; Dai and Trenberth 2004; Sun et al. 2006). This problem may be due in substantial part to issues in the convection parameterization schemes and their interactions with the large-scale dynamics in the models.

Retrieved statistics of rainfall, similar to those reported in, for example, Bretherton et al. (2004), Peters and Neelin (2006, hereafter PN06), and Neelin et al. (2009, hereafter NPH09) can be used to constrain climate models and convective parameterizations. Bretherton et al. (2004) analyzed satellite microwave retrievals on daily and monthly time scales and found an exponential relationship between conditionally averaged precipitation and column-relative humidity. Examining conditional averages of

Corresponding author address: Sandeep Sahany, Dept. of Atmospheric and Oceanic Sciences, University of California, Los Angeles, 405 Hilgard Ave., Los Angeles, CA 90095-1565.
E-mail: sandeep@atmos.ucla.edu

DOI: 10.1175/JCLI-D-13-00747.1

© 2014 American Meteorological Society

microwave retrievals of precipitation on column water vapor (CWV)—both essentially instantaneous in time—PN06 noted a rapid precipitation increase beyond a threshold value of CWV, much as one might expect from onset of convective conditional instability in a deep convection parameterization. Holloway and Neelin (2009, hereafter HN09) used in situ observations to evaluate this relationship to onset of conditional instability and further showed that inclusion of substantial entrainment in the convective instability calculation was important to correctly obtain the pickup in precipitation. CWV was shown to be a reasonable proxy variable for the effect of environmental lower-tropospheric moisture on conditional instability of an entraining plume, for which deep convective instability typically occurs only for sufficiently moist environment [as also noted in, e.g., Brown and Zhang (1997); Kuang and Bretherton (2006); Del Genio and Wu (2010)]. NPH09 used precipitation and CWV from satellite retrievals and tropospheric temperature from reanalysis to provide a quantification of the role of tropospheric temperature in governing the onset boundary for strong deep convection and to examine related convective transition properties.

In analyzing a complex system, such as deep convection, interacting with the large scale, guidance from simpler prototypes can be useful. PN06 noted that the statistics have sufficient similarities to certain aspects of continuous phase transitions and related critical phenomena that this analogy could be used to suggest a set of interrelated properties to seek in the observations. These include clusters, power-law spatial and temporal correlations, and power-law event size distributions in measures of the smaller-scale convection (such as precipitation or cloud water) occurring near the onset of conditional instability at a critical value, w_c, of large-scale CWV. A natural next step was a model whose relationship to atmospheric prognostic equations could be more easily seen and in which the relationship to observed probability density function (PDF) of CWV could be quantitatively examined. Stechmann and Neelin (2011) showed that a prognostic water vapor equation stochastically forced across a parameterized precipitation onset exhibits properties including power-law ranges in temporal correlation and event size distribution and that reasonable matches to the observed estimates of PDFs of CWV arise straightforwardly from a Fokker–Planck equation in which precipitation acts as the drift term. Many of these properties can be interpreted in terms of a first-passage process (Stechmann and Neelin 2014) with stochastic forcing across thresholds for precipitation onset/termination. The forcing across this threshold can occur substantially by large-scale processes, suggesting that it should be possible to capture these PDFs reasonably well in climate models, even without a stochastic convective parameterization [for review see, e.g., Neelin et al. (2008)], as will be addressed in part here.

In pragmatically assessing climate models against such statistics, one of the more important characteristics is to correctly capture the transition from shallow to deep convection. Sahany et al. (2012, hereafter SNHN12) showed that the pickup in precipitation and the location of the onset of deep convection were simulated reasonably well with a relatively high-resolution (0.5°) version of the Community Atmosphere Model (CAM3.5), primarily due to stronger entrainment rates included in the Neale–Richter (Neale et al. 2008) modified version of the Zhang and McFarlane convection scheme used in the model. The stronger entrainment led to the deep convective plumes becoming more sensitive to the ambient humidity of the environment (as represented by the model gridbox average moisture), such that instability for deep convection occurs only at higher free-tropospheric water vapor.

Both atmospheric water vapor content and global-mean precipitation are expected to increase under global warming, but the changes in spatiotemporal distribution of rain rates are more important for societal impacts. Allan and Soden (2008) found that heavy rain events in satellite observations increased during warm periods and decreased during cold periods, but at a rate higher than that predicted by models. Chou et al. (2009) noted a general tendency for tropical precipitation anomalies in climate models under global warming to follow the ''rich get richer'' effect (Chou and Neelin 2004; Held and Soden 2006) of increased precipitation in regions of climatological moisture convergence, although with regional-scale departures. O'Gorman and Schneider (2009) found that, although theoretically the intensity of precipitation extremes is expected to increase (e.g., within high percentiles of daily rainfall) with increase of column water vapor under global warming, there is significant disagreement in regard to tropical rainfall extremes among climate models from phase 3 of the Coupled Model Intercomparison Project (CMIP3). For both precipitation extremes and their fractional changes under global warming, the intermodel scatter in the tropics was found to be larger than that in extratropics. Muller et al. (2011) and Romps (2011) used convection-resolving models under idealized radiative–convective equilibrium and found that intense precipitation increases with warming at close to the rate expected from Clausius–Clapeyron scaling. Sun et al. (2007), Chou et al. (2012), and O'Gorman (2012) each reported increases in simulated intensity of extreme precipitation events (for instance, in upper percentiles of daily precipitation) over many regions under global warming conditions, although

the latter found strong disagreement between climate models on the rate of increase over the tropics.

Changes to the temperature profile under global warming will also prove relevant to our results. Santer et al. (2005) found amplification of surface temperature changes in the tropical upper troposphere in both observations and climate models over monthly time scales. However, over decadal time scales, while the model behavior was similar, there was lack of general agreement among the observational datasets. Chou et al. (2013) used model output from the CMIP3 and CMIP5 archives and found an increase in gross moist static stability over the tropics under global warming conditions.

Here we analyze output from uncoupled and coupled versions of the National Center for Atmospheric Research (NCAR) Community Climate System Model, version 4 (CCSM4), for both present-day and global warming conditions for the high emission scenario representative concentration pathway 8.5 (RCP8.5) to investigate tropical precipitation transition statistics simulated by the model. This is the first time such precipitation transition statistics have been analyzed for a coupled model, both in the current climate and under global warming. Analysis for the uncoupled model (CAM3.5) is presented in section 2 (which includes methodological details and caveats on aspects of the retrievals for readers who might want to reproduce these figures as process-oriented diagnostics for their climate model of choice). Analysis for the coupled model (CCSM4), including changes under global warming, is presented in section 3. We analyze several aspects of precipitation transition statistics, including the sharp pickup (PN06 and NPH09), probability of occurrence of CWV for precipitating grid points, and the convective onset boundary on an empirical temperature–CWV thermodynamic surface for the historical and RCP8.5. The simulated precipitation transition statistics for the historical period are compared with the corresponding retrievals from the Tropical Rainfall Measuring Mission (TRMM; Kummerow et al. 2000) Microwave Imager (TMI) processed by Remote Sensing Systems (RSS) with the Hilburn and Wentz (2008) algorithm [an updated version of Wentz and Spencer (1998)], and temperature profiles from the ERA-40 dataset (Uppala et al. 2005). The precipitation transition statistics under global warming are then analyzed to help understand simulated changes in the properties of deep convection compared with those of present day. Behavior tends to be similar for different tropical ocean basins (NPH09, SNHN12), so examples from the eastern and western Pacific are presented. In section 4 and the appendix, an entraining plume model similar to HN09 has been used for buoyancy computations to explain the characteristics of the convective onset boundary on the empirical thermodynamic surface for historical and global warming conditions.

2. Deep convective transition characteristics from high-resolution CAM simulations

a. *Precipitation pickup and estimation of onset boundary*

Figure 1a shows conditional average precipitation rate as a function of CWV binned at 0.3-mm intervals for a range of bulk tropospheric temperatures $\hat{T}$ (mass-weighted average over 200–1000 hPa) binned at 1-K intervals over the tropical eastern Pacific for the TMI conditioned with ERA-40 temperature profiles for the period 1 January 1998 to 31 August 2002. Similar to what has been discussed in previous related work (PN06; NPH09; SNHN12), the conditional average of the precipitation rate retrievals approaches a power-law relationship $a(w - w_c)^{\beta}$, where w is CWV, w_c a threshold value and a is an amplitude factor. Similar analysis for a high-resolution (0.5°) version of the NCAR CAM 3.5 (note, the convective physics of CAM3.5 is very similar to CAM4, the atmospheric component of CCSM4), analyzed for the period 28 December 1994 to 1 January 2000, yields good agreement with observations, although the power-law exponents differ for the two cases. The almost linear pickup (i.e., $\beta \approx 1$) seen in most model cases (departures are discussed below) is primarily related to convective closure assumptions in the convective parameterization scheme, in which a linear relationship between cloud-base mass flux and the entraining convective available potential energy (CAPE) is assumed. A relatively linear pickup of precipitation as a function of CWV has been noted in some cloud-resolving model simulations (S. Krueger 2014, personal communication) over limited time and space domains. These include a 5-yr GCM simulation using the multiscale modeling framework, which uses embedded 2D cloud-resolving models (CRMs) (with a domain size of 256 km).

We emphasize, as noted in NPH09 and SNHN12, that one should be cautious in interpreting the microwave retrievals at high water vapor and precipitation. The retrieval estimates cloud water in the column, and the retrieved precipitation rate is based on empirical relationships between cloud water and columnar rain rate (Hilburn and Wentz 2008; Wentz and Spencer 1998). Fewer occurrences of very high rain rate and CWV cases suggest that calibration will tend to be less reliable at high values. For instance, Seo et al. (2007) showed that the TMI-derived rain rates are underestimated by more than 50% at precipitation radar (PR)-derived rain rates of greater than 25 mm h^{-1}. Furthermore, CWV is not directly retrieved above rain rates of about 15 mm h^{-1}, and 25 mm h^{-1} is considered an extreme upper bound on

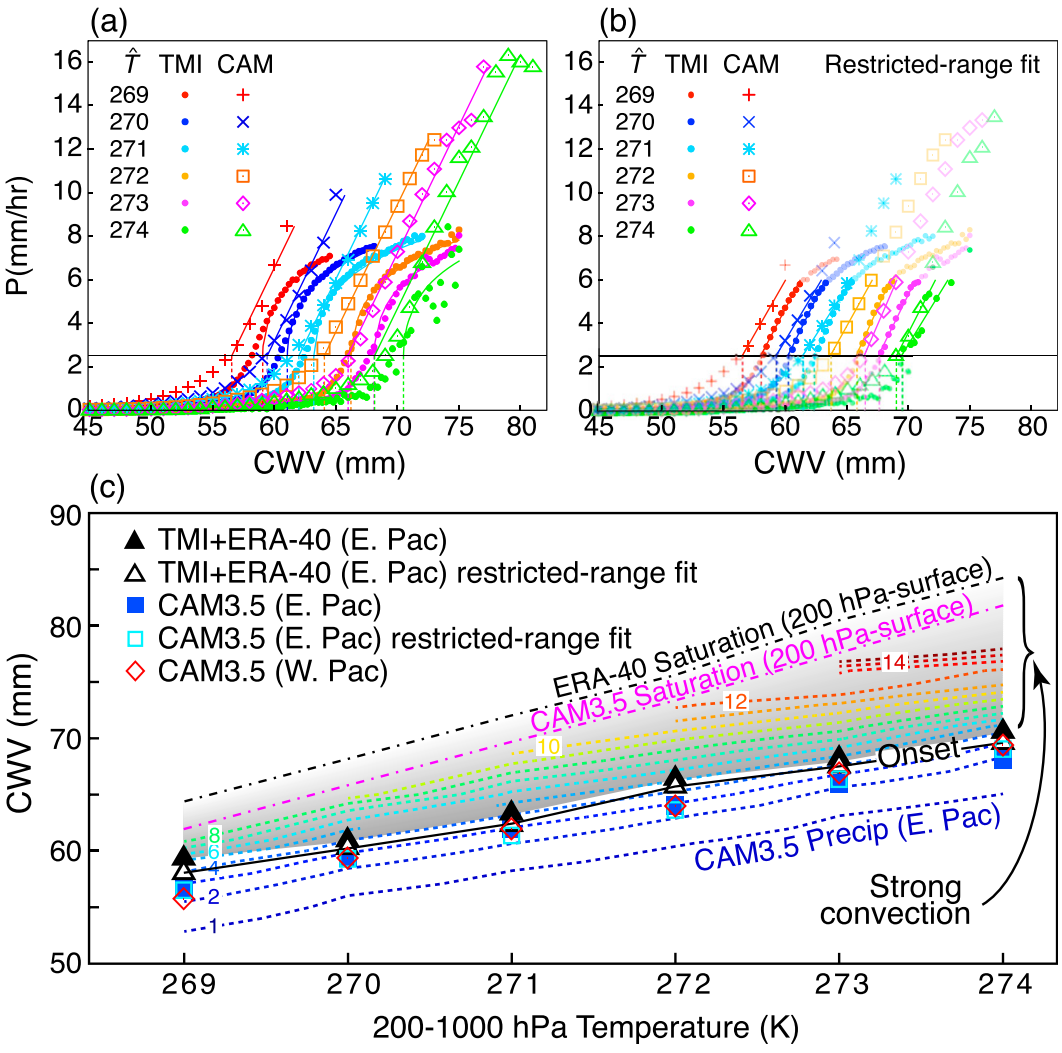

FIG. 1. (a) Conditional average precipitation as a function of CWV for different bins of $\hat{T}$ over the tropical eastern Pacific from TMI using the ERA-40 temperature profiles and a 0.5°-resolution version of CAM3.5. Power-law fit lines (solid curves, see text) are shown above the critical value w_c, where precipitation undergoes a rapid increase (vertical dashed lines starting at $P = 2.5\,\mathrm{mm\,h^{-1}}$ connect the fit curves to the estimates of w_c on the x axis). A power-law exponent of 0.23 is fit for the TMI retrieval, whereas for the model it is 1. (b) As in (a), but for a linear fit over a restricted range. (c) The critical column water vapor w_c from retrievals (TMI) and model (CAM3.5) as a function of bulk tropospheric temperature $\hat{T}$. Critical values from two fitting methods, corresponding to (a) and (b), are shown for eastern Pacific TMI and CAM3.5. Western Pacific values from CAM 3.5 are shown for the first method. Contours of CAM3.5 conditional average precipitation are shown in background (dashed lines). Also shown for reference are the values for column saturation (dashed–dotted) from both ERA-40 and CAM3.5.

the algorithm's ability to retrieve rain (Wentz and Spencer 1998). Thus, the apparent curvature in the retrievals at high CWV may well be associated with saturation of cloud water or retrieval error and does not constitute a basis for comparison to the model. Rather, it is the location of the strong pickup that is of leading interest for model validation (and properties near this onset). PN06 checked the effects of using cloud water rather than precipitation retrievals and obtained very similar values for the estimated w_c. See HN09 for verification of the onset dependence for the Atmospheric Radiation Measurement (ARM) Program (Stokes and Schwartz 1994; Mather et al. 1998) in situ (optical rain gauge and radiosonde) observations over the tropical western Pacific.

A practical issue with asymptoting to a linear pickup is that the fitting procedure in the model can be prone to be affected by the "foot" region of transition from very low conditional average precipitation at low CWV into the pickup regime. In CAM, there is a deterministic relationship between cloud-base mass flux and entraining

CAPE that yields zero below a threshold value and then a linear increase. As outlined in NPH09 and HN09, CWV serves as a reasonable proxy for the water vapor effect on CAPE when there is sufficient entrainment, but unaccounted vertical degrees of freedom in using bulk measures of tropospheric temperature and moisture can act in a manner similar to a stochastic effect that smooths the onset in this foot region. To provide a clearer example of this, following Eq. (4) of NPH09, the conditional average precipitation will have effects that look approximately like the following:

$$\langle P \rangle = \int P_0(w_* + \xi) p(\xi)\, d\xi', \tag{1}$$

where $w_* = w/w_c(\hat{T})$. The function P_0 represents the precipitation as a function of w_* under idealized conditions where vertical structures and other factors are controlled to only change in a highly prescribed manner such that the single vertical degree of freedom represented by CWV and $\hat{T}$ approximately captures the water vapor–temperature dependence. The effects of departures from this idealized condition are summarized in ξ, which in the model is deterministic if the large-scale state is precisely known, but which can appear like a stochastic effect when one cannot control for all possible variations, with $p(\xi)$ the PDF of ξ as it occurs in the model simulation. Because P_0 will tend to look like the ramp function (zero then linear) that is built into the entraining CAPE dependence, this smoothing effect will tend to produce conditional average precipitation that is larger than P_0 on the low CWV side of the pickup by averaging in some values from above the onset. Effects at high CWV will be discussed below. Similar effects plus measurement error would contribute in observations, but the foot region is systematically narrower in the retrievals than in the model (suggesting some combination of the model exaggerating this effect relative to observations and the retrieval errors not being so large as to compensate). To seek fitting techniques that characterize the strong pickup at the grid resolution while avoiding bias from the foot region and differences in curvature, we checked several variants of the procedures used in PN06, NPH09, and SNHN12.

In a first of two main variants, we estimate w_c by estimating a power-law fit above a threshold precipitation value of $2.5\,\mathrm{mm\,h^{-1}}$ and defining w_c as the value at $2.5\,\mathrm{mm\,h^{-1}}$. Applying the threshold helps to keep the fit outside the range of the foot discussed above (although if applied to a new model or dataset this should be verified). Defining w_c at a precipitation threshold value greater than zero aims to accurately characterize the rapid onset of strong precipitation. This will tend to be at a slightly higher-CWV value than where one might find the zero of the ramp function in the parameterization, but it avoids attempting to extrapolate a fit that would be prone to error in the presence of the foot. Within this fitting approach, we tested impacts of fitting individual values of β for each $\hat{T}$ versus using a single value that best fits the curves with most data (as shown in Fig. 1a) or changing the threshold. The differences associated with different estimation procedures tend to be typically 1 mm or less. The case shown also requires a minimum of 5 data counts in each conditional average.

In the second variant, referred to as the "restricted-range fit," we specify both an upper and lower bound for conditional average precipitation, 2.5–$6\,\mathrm{mm\,h^{-1}}$, and use a linear fit within this range, defining w_c as a value at $2.5\,\mathrm{mm\,h^{-1}}$ as before. This fit is then iterated to include only a 5 mm CWV range above w_c, as a safeguard against possibly noisy points at high water vapor where there are few counts. The range in both precipitation and in water vapor is narrow enough that differences in curvature at high water vapor and high precipitation tend to be excluded. This proves to be highly relevant not only for model to microwave retrieval comparison, but also within the model itself, since curvature of the model conditional average precipitation curve turns out to be substantial in global warming runs discussed below. One could consider using a narrower range, or even interpolating across $2.5\,\mathrm{mm\,h^{-1}}$, but this would be prone to estimation effects in cases with shorter datasets or at high temperatures where there are fewer counts (a requirement of 10 counts in each point is illustrated here). Figure 1b shows results of this restricted-range fitting method. As expected, the critical values are very similar to those obtained by the first method, although they do tend to move the CAM and TMI values slightly closer, due in large part to fitting over an approximately linear range in both. Effects of increasing the threshold number of data points in a bin from 5 in Fig. 1a to 10 in Fig. 1b are also evaluated, impacting a few of the highest ensemble-average precipitation values for $\hat{T}$ values of 273 and 274.

We display these values as an onset curve shown on a temperature–water vapor thermodynamic plane (Fig. 1c) similar to that shown in NPH09 and SNHN12. The critical value w_c is seen to have a simple dependence on the bulk tropospheric temperature, increasing approximately linearly with $\hat{T}$ both in observations and the model, at a rate slower than that of column saturation. Model results have a similar behavior to that seen in observations for both fitting methods. The separation from saturation is due to the onset of conditional instability for deep convection typically occurring before the environment is fully saturated (as measured by the average across the grid cell). It was suggested in SNHN12 that the slope in the temperature–water vapor plane depends on a number

of factors, including the vertical profile of the temperature changes and, importantly from the point of view of model validation, the representation of entrainment in the model convective parameterization. With sufficient entrainment in the lower free troposphere, the observed onset boundary could be approximately matched. SNHN12 argued that this is consistent with entrainment providing the mechanism that yields the observed sensitivity to environmental water vapor above the boundary layer. Figure 1c also shows the onset curve for the tropical western Pacific as an indicator of how similar the results are for different tropical basins (see SNHN12 for comparison to Atlantic and Indian cases in CAM and PN09 and NPH09 for comparison in retrievals). For brevity, the tropical eastern Pacific is used as an example for most onset figures, returning to western and eastern Pacific comparisons (see Fig. 6), where the eastern Pacific shows more distinct changes in frequency of occurrence of rescaled CWV for precipitating points.

The estimated w_c values in the model are slightly lower than those for observations for the entire range of tropospheric temperatures analyzed, even after the modified procedure is used, and this is consistent with visual inspection of Fig. 1a, where the rapid pickup of precipitation typically occurs at a slightly lower water vapor for each temperature. However, for a given $\hat{T}$, the model column saturation value is slightly lower than the observed because of differences in mean vertical structure, so the subsaturation is more comparable. Furthermore, considering how easy it is for this onset curve to be dramatically off from the observed if entrainment is changed (SNHN12) and that the model was never tested against the statistics during the tuning process, the agreement of this onset curve is impressive.

Contours of conditional average precipitation in Fig. 1c emphasize that the onset curves lie parallel to the precipitation contours in the region of strong gradient. For temperatures where there are high data counts, the fitting methods give onset curves very similar to a 2.5 mm h^{-1} precipitation contour. The difference in the estimated w_c values from the two fitting methods for the TMI observations averaged over all $\hat{T}$ values is about 0.8 mm. This difference can also be visualized in Fig. 1c as the narrow white region between the solid black line and the shaded region above. For the model, as expected, the alternative fitting method does not introduce much difference in the estimated w_c values: only −0.03 mm averaged over the $\hat{T}$ range used. Comparing the difference between the estimated critical values between TMI–ERA-40 and CAM3.5 for the restricted-range fit the average value is 1.2 mm, less than half of the corresponding difference in column saturation values (2.7 mm) between the model and ERA-40, owing to differences in their vertical temperature structures. In short, the model matches the onset boundary of the retrievals about as well as can be currently expected. Given the similarity of the results for both fitting methods, subsequent plots will display results using the first method, with values from the second method discussed where appropriate.

b. *Frequency of occurrence (PDFs)*

Figure 2 shows the PDF of column water vapor rescaled by the corresponding critical values for each of the $\hat{T}$, considering only the precipitating points. The distributions are shown as occurrences in each bin of 1°C in $\hat{T}$ and of 1 mm (TMI) or 0.5 mm (CAM) in CWV. They have been displayed as the number of counts instead of normalizing (either across CWV for each $\hat{T}$ or across both variables), because normalization corresponds to a simple vertical shift of each curve in the logarithmic y axis, and the absolute number of occurrences is also relevant. Compared to normalization for each $\hat{T}$, this choice also spreads the curves in the y-direction and allows the relative importance of each $\hat{T}$ to be seen. Because the shape is not altered if one were to switch to units for a normalized probability density function, in the following discussion, we use the term PDF interchangeably to refer to these curves.

Figure 2a is similar to that shown as Fig. 5b in NPH09. As discussed in NPH09, the occurrence frequency features a Gaussian core with a peak near the critical value (around 0.9), and a longer-than-Gaussian tail on each side that over a certain range can resemble an exponential decay. The long tail above w_c is associated with much more frequent excursions into the heavy precipitation regime than one would expect from extrapolation of the Gaussian core and thus is of interest for understanding occurrence of extreme events. As emphasized in NPH09, due caution is needed in interpreting microwave retrievals in the high precipitation regime. This is further discussed in section 2c, since these PDFs potentially represent a significant point of comparison for models.

In Fig. 2b we show a similar figure using the 0.5° CAM3.5 precipitation and column water vapor binned by $\hat{T}$ values computed at a coarse resolution of 2.5°, to make a more direct comparison to the observations. The overall shape of the distribution is very similar to that observed, although there are also differences. The Gaussian core near points below w_c is clear in the model output. Within the region above this, just below w_c, we can distinguish two regimes. From slightly below critical (around 0.95) up to w/w_c values of around 1.1, there is an interval in which the occurrence probability decreases much less quickly than would be suggested by the Gaussian core. This is the regime that corresponds to the longer-than-Gaussian tail seen in observations. At values

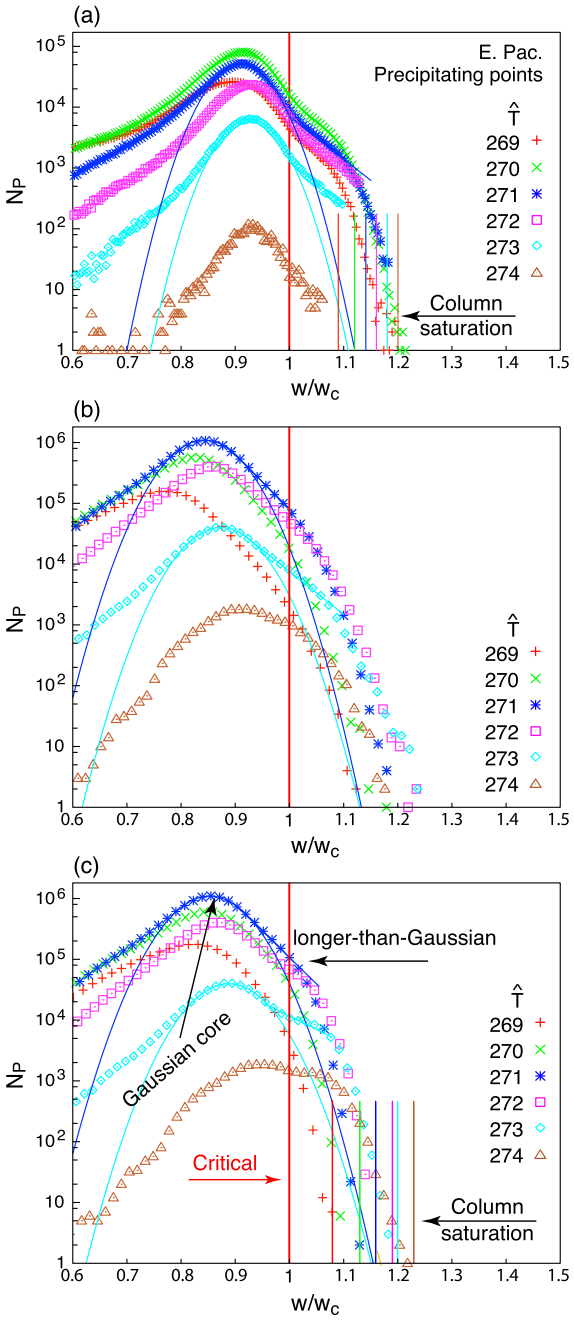

FIG. 2. Log-linear plot of the frequency of occurrence (N_p) of CWV rescaled by the corresponding onset threshold values $w_c(\hat{T})$ for precipitating points over the tropical eastern Pacific binned for $\hat{T}$ values at 1-K intervals (curve shapes are the same as PDFs, aside from a shift corresponding to a normalization constant). (a) TMI precipitation and column water vapor binned by ERA-40 temperatures, (b) 0.5° CAM3.5 precipitation and column water vapor binned by bulk tropospheric temperatures computed at a coarsened resolution of 2.5° for a better comparison with (a), and (c) 0.5° CAM3.5 precipitation and column water vapor binned by bulk tropospheric temperatures computed at native model resolution. Gaussian fits (parabolas) to the core and exponential fits (straight lines) to the tail are shown for selected $\hat{T}$ curves to aid comparison. Vertical bars indicate column saturation values corresponding to $\hat{T}$ values of the same color.

greater than about 1.1, the occurrence probability drops quickly, corresponding to the regime where column saturation has been encountered. In other words, the longer-than-Gaussian tail occurs in the interval between the onset of conditional instability and column saturation. The cutoff near saturation may be seen more clearly in Fig. 2c, where the native model resolution is used to compute the $\hat{T}$ values. A similar feature is seen in the retrieval analysis for $\hat{T}$ = 269–270 K, associated with a consistency check in which instantaneous cases for which CWV from TMI exceeds column saturation from ERA-40 are excluded in the computation. For $\hat{T}$ = 272–274 K, a retrieval algorithm internal cutoff at 75 mm limits the upper end of the TMI values.

c. *Caveats and interpretation of model–retrieval comparison*

In section 2a, concerns regarding high rain-rate microwave retrievals were treated by showing that the onset boundary for rapid precipitation pickup is robust to exclusion of these. For the PDFs in Fig. 2, this is the first comparison to climate model results, and the high-CWV regime will prove of interest in the global warming behavior (section 3), but the CWV retrievals can have nontrivial errors in the precipitating regime. A brief discussion of caveats and the extent to which the model provides interpretation of retrieval PDF features is appropriate.

Regarding the existence of a Gaussian core with longer-than-Gaussia tails, there are a number of lines of corroborating evidence that these represent physically reasonable behavior regimes. Neelin et al. (2010) discuss how such long tails are typical of a class of tracer advection problems with a maintained gradient (Pierrehumbert 2000; Bourlioux and Majda 2002; Majda and Gershgorin 2013), and can be found in PDFs for chemical tracers in models and independent retrievals. This establishes a simple mechanism that would apply to CWV distributions generally (not just precipitating points.) Lintner et al. (2011) examine the relationship of such tails in water vapor distributions to circulation using a number of datasets.

In CAM, the simulation of corresponding core/tail behavior for CWV PDFs for precipitating points suggests that these features are reasonably straightforward to obtain, at least in a model that can realistically simulate the position of the convective onset boundary relative to column saturation (since the long tail exists in the interval between these). It is worth noting that this is an emergent behavior for which the model has never been examined or tuned. The width of the Gaussian core is comparable to that of the retrievals. The PDFs in the model differ somewhat more in terms of the shape for different $\hat{T}$ than is seen in the microwave retrievals, especially for the tail for the lowest and highest temperatures.

In assessing at what level of detail the retrievals can be trusted, it is useful to consider what aspects of convective-scale or large-scale physics might contribute to the PDF, as well as sources of retrieval error. In the simple model of Stechmann and Neelin (2011), similar distributions could be mimicked by including the following: (i) a CWV-dependent precipitation pickup; (ii) a stochastic representation of large-scale (i.e., larger than grid-scale) moisture convergence; (iii) a stochastic precipitation component assumed to arise from subgrid-scale effects; and (iv) a stochastic transition from shallow to deep convection that represents the effects of degrees of freedom not captured by grid-scale CWV. The Gaussian core depends quantitatively on all four, while the high-CWV tail depends primarily on the first three. They note that the effects of (ii) and (iii) were largely indistinguishable, while Stechmann and Neelin (2014) show that simplifications without (iv) can capture qualitative aspects in some circumstances. In CAM, the convection parameterization is deterministic, and precipitation rate depends on the entraining CAPE with a specified adjustment time scale. One can infer that the shape of the CAM PDF must thus be due to large-scale forcing pushing the column thermodynamic conditions back and forth across the conditional instability onset boundary for deep convection, with occasional events strong enough to push the system farther than typical above this onset despite the 1-h dissipation time scale. Near the onset boundary, the effects of vertical degrees of freedom that affect entraining CAPE but are not controlled for by CWV and $\hat{T}$ would tend to impact the PDFs diagnosed as a function of these quantities.

In observations, each of these physical processes can be expected to play a role, but imperfectly known retrieval errors can also affect the PDF. The procedure for estimating variations of retrieved CWV against radiosondes is limited in part by differences associated with mismatches in spatial and temporal colocation and point observations versus spatial averages. In raining conditions, an estimated 3.7 mm must accordingly be discounted from the 5-mm root-mean-square (RMS) difference between retrievals of spatially averaged water vapor and neighboring sonde points, implying a little over 3 mm from other sources (Wentz and Spencer 1998). Conservatively taking this as translating to a random error standard deviation 0.05 in w/w_c would suggest that CAM (with no random error) is simulating an overly wide core. However, Lintner et al. (2011), using independent upward-looking radiometer instrumentation at Nauru, find CWV PDFs for precipitating points with widths comparable to those seen here. Furthermore, most of the remaining 3 mm RMS in the satellite microwave retrieval–radiosonde differences is not random instrument error but, rather, comes from variations of hydrometeors and water vapor at smaller spatial scales than the horizontal and vertical spatial averaging footprint of the retrieval. These thus represent an atmospheric signal of small-scale variations (i.e., of one of the physical effects that contributes to core width in CAM). Overall, until the microwave retrievals can be further calibrated for these purposes, quantitative differences between model and retrieval PDFs should be viewed with caution. The model results for changes in these PDFs discussed in section 3 may motivate such calibration efforts. Lastly, we note an ambiguity in the appropriate spatial scale for comparison. In section 3, we use an approximately 1° version of the model (versus 0.5° in this section). Similar results are obtained at the respective grid scales, presumably because the parameterized convective plumes interact with grid-scale moisture and temperature such that the model behaves similarly at the smallest scales available to it. Systematic assessment across resolution would be desirable in future; here we provide a first assessment of changes in these statistics at the available resolution.

3. Changes in convective transition statistics and onset threshold under global warming

a. Precipitation pickup and critical surface

Precipitation pickup over the tropical eastern Pacific similar to Fig. 1 is shown for 20-yr time intervals from the historical (Fig. 3a) and RCP8.5 (Fig. 3b) runs for the NCAR CCSM4 from the CMIP5 archive. For the historical run, model output is analyzed for the period 1981–2000. For a given $\hat{T}$ bin, the conditional average precipitation rates do not reach quite as high values as the corresponding 0.5° values for similar CWV because of the coarser 1° resolution. The precipitation pickup for the different $\hat{T}$ bins is similar to that seen in Fig. 1a. The curvature seen for the highest CWV bin will be discussed below.

For the RCP8.5 run, the 20-yr period corresponding to the end of the century (EoC; 2081–2100) has been analyzed. The mean warming for the region is about 4 K, so the curves for 273–278 K in Fig. 3b are most comparable to those shown for the historical run in Fig. 3a. To facilitate comparison to the onset values for the historical run, curves are included for a larger range of temperatures, displaying bins from 270 K, even though this temperature is now uncommon in the warmer climate. In Fig. 3b it can be seen that the pickup in precipitation shifts to higher values of CWV for warmer temperatures, as expected qualitatively. Quantification of how the onset shifts will be analyzed in more detail by comparing the increase in w_c with $\hat{T}$ in the historical and end-of-century case. In particular, it

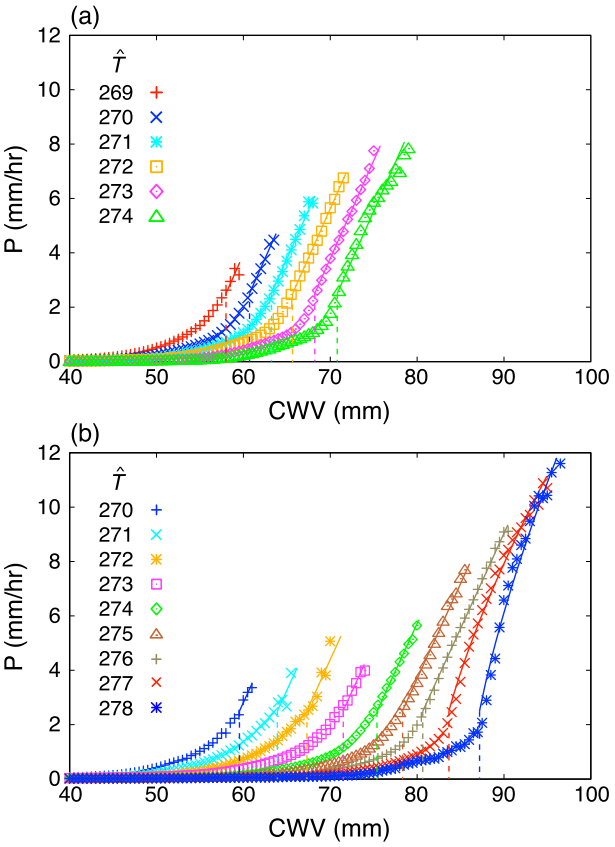

FIG. 3. Precipitation pickup for 1° CCSM4 over the tropical eastern Pacific, similar to Fig. 1a: (a) historical (1981–2000), and (b) EoC (2081–2100) for the RCP8.5 scenario.

will be of interest to know how this increase compares to that given by a constant relative humidity case, in which the moisture content of the atmosphere increases at around 7% K^{-1} by the Clausius–Clapeyron equation (Trenberth et al. 2005; Dai 2006; Soden et al. 2005).

Before doing this, we note that the curvature of precipitation rate at high values of CWV in the warmest two $\hat{T}$ bins is so substantial in the global warming case that a linear fit does not work well over the full range above w_c. These are thus fit with $\beta = 0.7$. Using the restricted fitting-range approach of Fig. 1b continues to work well in this circumstance and gives very similar values of w_c. One simple argument that can explain this curvature is related to the effect that gives smoothing at the foot of the pickup, described in Eq. (1). Since CWV and $\hat{T}$ do not contain full information about the temperature and moisture vertical structures that affect the onset of conditional instability, variations of these can create departures that at high CWV will tend to be biased toward sampling less unstable conditions and reducing the conditional average precipitation. A numerical example of the effects summarized in Eq. (1) may be seen in Muller et al. (2009), producing a curvature comparable to that seen in Fig. 3b. One would expect stronger curvature at higher values of $\hat{T}$ to be associated with larger variations, and this appears to be consistent with effects seen in PDFs of precipitating points discussed in section 3b. However, because there is limited confidence in how to determine curvature for surface precipitation at high CWV from the available observations in the present day, we simply note this effect as a possibility for future investigation.

We further note that, in addition to a higher conditional average precipitation at high water vapor and temperature in the global warming case, precipitation variance increases strongly. In the historical run, precipitation variance tends to peak or plateau slightly above critical, with peak value tending to increase with temperature (figure not shown). In the global warming case, the corresponding $\hat{T} + 4\,K$ curve has roughly 3 times the peak value of variance as its counterpart in the historical run. Because this occurs in the supercritical range, we are cautious regarding possible observational constraints on this behavior, but we note it because other precipitation extreme event statistics in the model would be likely to reflect it.

We now return to the leading-order question of how the onset of convection changes. Figure 4a shows the precipitation pickup from the historical run for each of the $\hat{T}$ bins shown in Fig. 3a, but as a function of the rescaled column water vapor (w/w_c). The precipitation rates are also rescaled by the amplitude factor a of the power-law fit. The normalized pickup curves show a nice collapse for all the $\hat{T}$ values analyzed, thus confirming the usefulness of the rescaled parameter (w/w_c) and adding credibility to the procedure used to estimate the w_c values. This figure is similar to Fig. 2 of NPH09. Even under global warming conditions (Fig. 4b) the collapse still occurs for most of the $\hat{T}$ bins, excepting the highest bins (corresponding to the change in shape of the curve at the highest $\hat{T}$ seen in Fig. 3 for the EoC case discussed above) and noting that a larger range of $\hat{T}$ has been included to have some overlap between historical and global warming cases.

Figure 5a shows the deep convective onset boundary on a temperature–CWV thermodynamic surface, similar to Fig. 3a of NPH09. Important changes in the onset curves can be seen as one moves from current climatic conditions to a warmer climate. The deep convective onset shape under global warming has the same elements as in the historical case: at sufficiently high temperatures, it inclines away from the saturation curve with the separation between the onset of conditional instability and saturation increasing with $\hat{T}$. Note that a larger range of $\hat{T}$ values has been used for the global warming case to allow comparison with the corresponding values for the historical.

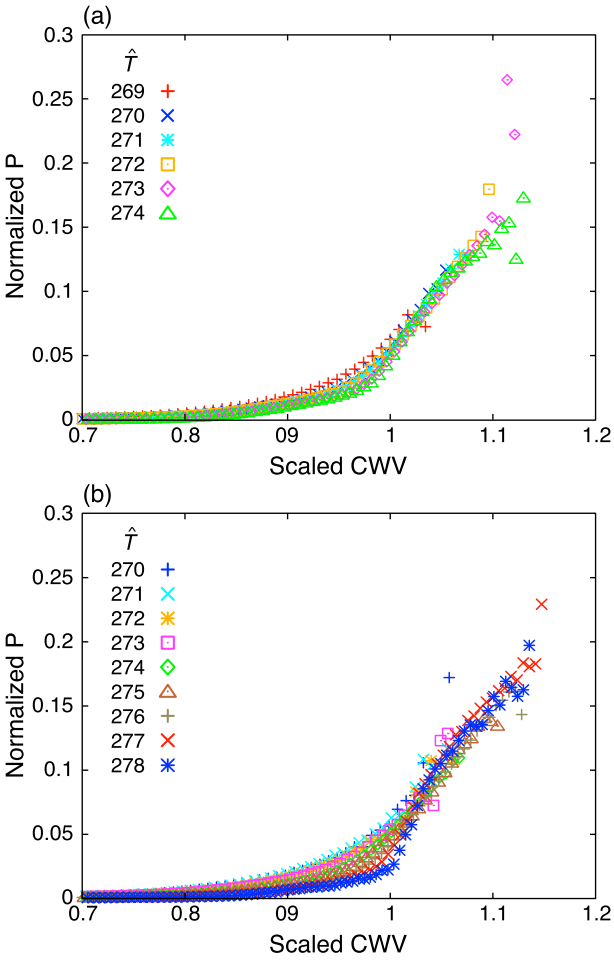

FIG. 4. Ensemble-average precipitation over the tropical eastern Pacific as a function of column water vapor rescaled by the corresponding w_c for each of the $\hat{T}$ bins at 1-K intervals: (a) historical and (b) EoC for RCP8.5 warming, showing the collapse of the curves over the range of $\hat{T}$.

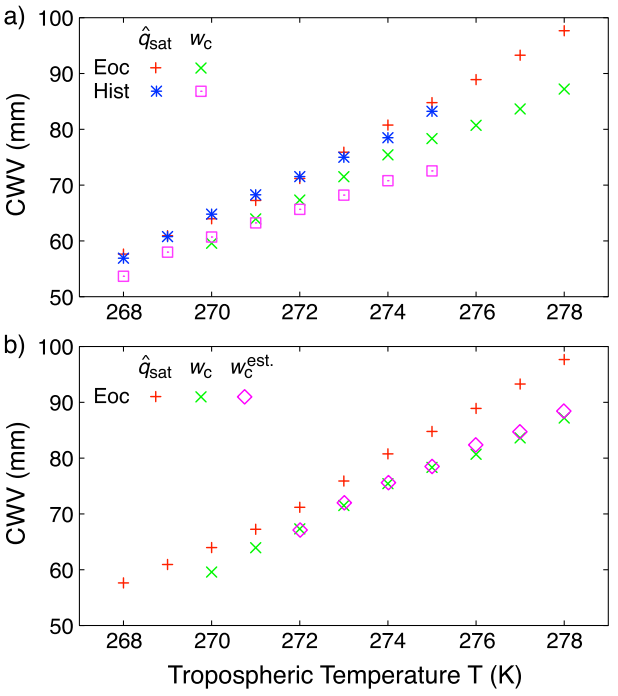

FIG. 5. (a) Deep convective onset boundary for the tropical eastern Pacific similar to Fig. 1b for the historical and EoC. Also shown for reference are the corresponding saturation values for the two cases. (b) As in (a), but only the EoC values are retained, and a new curve with w_c values is projected from the historical values by a simple conjecture. Specifically, the w_c projections are obtained by shifting the historical $\hat{T}$ by 4 K (approximate change in $\hat{T}$ over tropical eastern Pacific at EoC) and multiplying the corresponding historical saturation fraction by the EoC column saturation values for the shifted $\hat{T}$ (see text for details).

One of the simplest conjectures of how this shift in onset boundary under global warming occurs is a version of a constant relative humidity approximation. Defining a saturation fraction as w_c divided by the column saturation value for the same temperature, we examine whether adding 4 K (the average increase in $\hat{T}$ over the tropical eastern Pacific in CCSM4 during the EoC as compared to historical) to the historical $\hat{T}$ values and multiplying the saturation fraction of the w_c values by the corresponding saturation CWV (for $\hat{T}$ + 4 K) under global warming yields w_c estimates close to the ones shown in Fig. 5a. Historical values shifted by this method indeed yield critical values close to those estimated for EoC (see Fig. 5b). Section 4 provides an analysis of why this approximation works reasonably well using a simple conditional instability calculation with information about the CCSM change in temperature profile under global warming.

b. *Probability density function of precipitating points*

Figure 6 shows the occurrence frequency of precipitating points for the tropical eastern and western Pacific for the historical and RCP8.5 model outputs. The figure is similar to that shown in Fig. 2 for the observations and the uncoupled version of the model run at a higher resolution (0.5° CAM3.5). The curves on the panels are color coordinated such that a given $\hat{T}$ under the historical period has the same color and marker as the corresponding ($\hat{T}$ + 4 K) curve in the EoC. Since the average increase in $\hat{T}$ under global warming over the two basins is around 4 K, the curves of the same color represent similar temperatures relative to the mean of their respective climates and may reasonably be compared. In general, the curves for the most commonly occurring temperatures tend to exhibit a similar form of these PDFs for precipitating points for different values of $\hat{T}$, for both tropical eastern and western Pacific, and for both historical and the RCP8.5 global warming scenario, similar to that seen in observations and the uncoupled version of the model. The fact that normalization by w_c brings the main features of

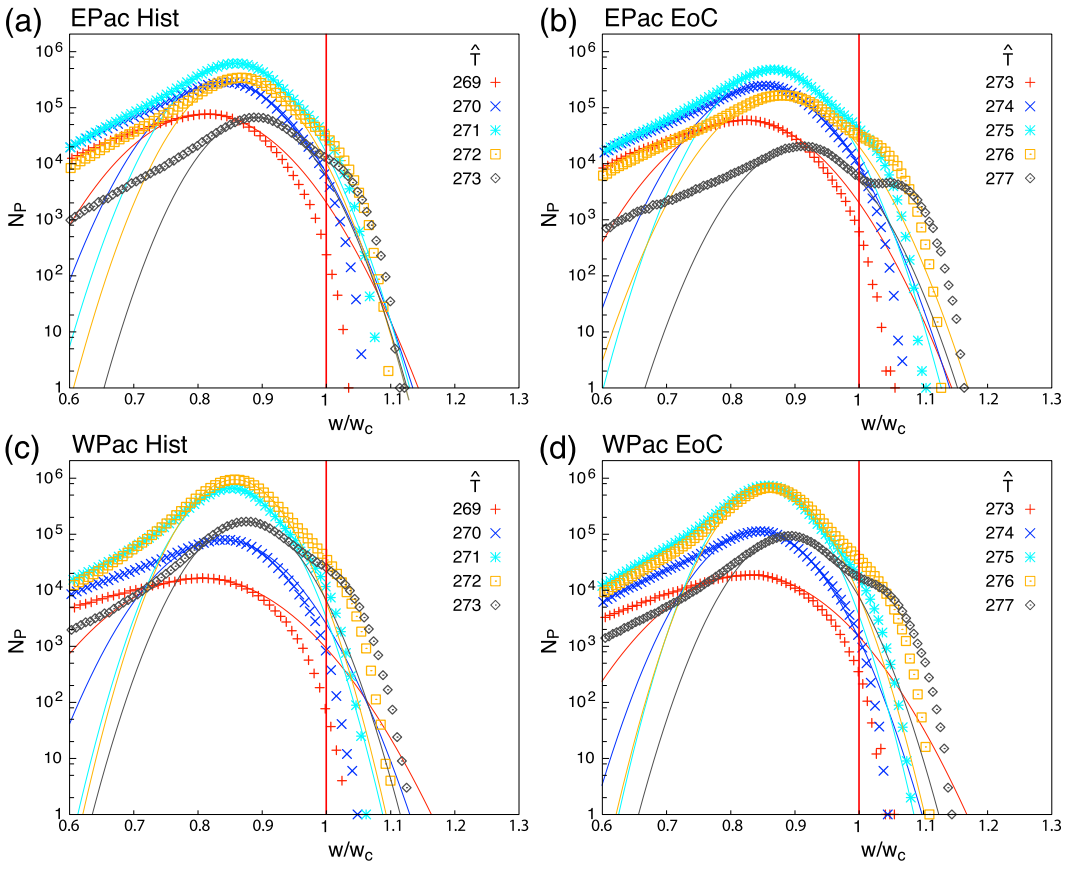

FIG. 6. As in Fig. 2, but (left) for the historical and (right) for the EoC for tropical (top) eastern and (bottom) western Pacific. As in Fig. 2, the procedure tends to collapse in occurrence statistics of rescaled column water vapor for precipitating points for different values of $\hat{T}$, confirming that the leading effects are controlled by the critical values.

the PDFs into line irrespective of resolution and ocean basin and for both coupled and uncoupled versions of the model adds to the credibility of the usefulness of critical column water vapor as a measure of the deep convective onset.

For the historical runs, the results are not very different from the uncoupled version, although it is at a coarser resolution (1° vs 0.5°). Comparing the model output for the historical and the RCP8.5 global warming conditions, it can be seen that the shift in the distribution to higher values of $\hat{T}$ under global warming is, to a first approximation, well predicted by the corresponding shift in the critical point, especially for the Gaussian core of the distribution. However, the global warming case (Figs. 6b,d) tends to exhibit a slight enhancement of the longer-than-Gaussian part of the range relative to the Gaussian part. It is particularly distinct for $\hat{T} = 277\,\mathrm{K}$ over the tropical eastern Pacific (see Fig. 6b) which almost has a second peak near saturation.

The increase in frequency of occurrence in the supercritical range (above w_c) appears consistent with changes in extreme events in a warmer climate noted in other studies (e.g., O'Gorman 2012), but gives a complementary view on the manner in which they arise. The critical point corresponds to the onset of deep convective conditional instability (Neelin et al. 2008), and in the climate model the convective scheme attempts to keep the system near this, with a time scale of 1 h for removing entraining CAPE. The supercritical range corresponds to dynamical driving strong enough to push the system beyond the typical convective quasi-equilibrium range represented by the Gaussian core. In the warmer climate, especially at the warmer temperatures, this occurs more often. This diagnostic does not yield an answer to exactly why this is occurring but helps to quantify its occurrence. In the model, when this occurs very strongly, it can push the system all the way to saturation (through some layer, which can occur slightly below column saturation), in which case large-scale condensation is activated in addition to the parameterized convective precipitation. This likely accounts for the peak near saturation for $\hat{T} = 277\,\mathrm{K}$ in Fig. 6b. While the specific way that this behavior in the supercritical range is represented in the model may be

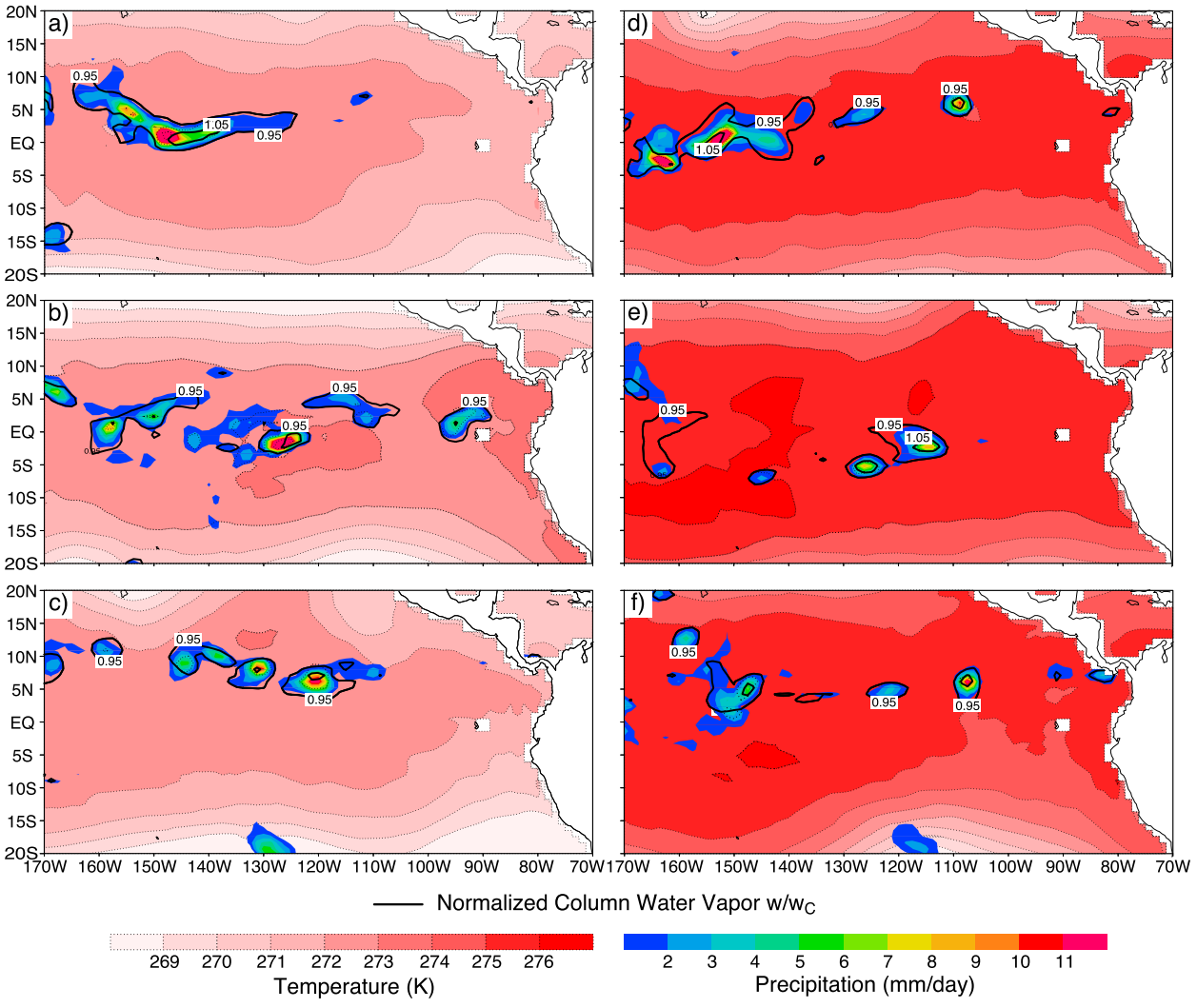

FIG. 7. Instantaneous snapshots of precipitation, $\hat{T}$, and rescaled CWV (w/w_c; with w_c linearly interpolated as a function of $\hat{T}$ for each of the grid points), for the (a)–(c) historical, and (d)–(f) EoC, in chronological order. Dotted lines with shading are for $\hat{T}$, solid lines with shading for precipitation, and solid black contours for w/w_c. The snapshots have been chosen from the tail of the distribution for the higher $\hat{T}$ from the historical and EoC such that each of them has at least one grid point with w/w_c near 1.1, representing the extremes.

imperfect, one may infer from the presence of a longer-than-Gaussian range in current climate in both model and retrievals that this is a representation of a real behavior regime that deserves additional scrutiny, as elaborated in the discussion.

c. *Events constituting the tail of the distribution*

To get a sense of the spatial structure of the events that constitute the tail of the distribution, especially for the higher $\hat{T}$ values that show significant changes under global warming, we examine maps of instantaneous precipitation and normalized CWV superimposed on maps of $\hat{T}$. CWV is normalized by the critical value corresponding to the temperature at that location: that is, $w/w_c(\hat{T})$ is calculated (with w_c linearly interpolated between $\hat{T}$ values) and displayed for selected contours near critical. Figure 7 shows representative snapshots from both historical and EoC simulations. The figures show large areas with w/w_c greater than 0.95, with localized pockets reaching values of 1.05 or higher. The location of peak precipitation generally coincides with those having highest values of w/w_c. The highest $\hat{T}$ values occur within the warm core of these storm-like features, an effect also seen in observations, although large temperature gradients are quickly damped out by wave dynamics away from strong storms. The convective events range from the more localized ones to well-organized synoptic-scale events, including some suggestive of easterly waves or tropical storms, and both larger and smaller convective cloud clusters. The basic

characteristics of these events appear not to be distinctly different under global warming conditions—high water vapor (relative to w_c) points simply tend to occur more frequently and at higher associated precipitation intensities than in the historical period.

4. A simple prototype for the shift in the convective onset boundary

The conjecture presented in Fig. 5b using the historical w_c values to predict those for the EoC works reasonably well, so it is useful to understand why in more detail. A set of plume buoyancy computations with a prescribed fractional entrainment rate, under idealized changes to the temperature and moisture profile, are carried out similar to a subset of those in SNHN12. Specifically, an air parcel is initialized with the temperature and specific humidity values of the idealized environment (discussed below) at the 1000-hPa level and ascends with a vertically constant fractional entrainment rate of 0.002 hPa^{-1} (case C2 from SNHN12), otherwise conserving its total water and ice-liquid water potential temperature. For the historical case, multiples of vertically constant temperature perturbations of 0.2 K are added to a base-state temperature profile over Nauru (an ARM observation site over the tropical western Pacific), obtained by averaging profiles conditioned on high values of CWV (>66 mm; see HN09 for details) representative of conditions favoring deep convection. Tropospheric relative humidity is varied in the range of 51%–99% in increments of 2% using a vertically constant profile above 800 hPa, and a blending region up to 950 hPa tapering (6.5% per 50 hPa) to a surface relative humidity value of 85% typical of deep convective cases over Nauru (HN09). Entraining CAPE contours of 100 J kg^{-1} are used as a measure of the deep convective onset boundary unless the free troposphere reaches saturation, in which case large-scale precipitation is assumed to onset.

The resulting precipitation onset boundary is seen in Fig. 8 as a function of CWV and bulk tropospheric temperature $\hat{T}$. At low values of $\hat{T}$, the onset curve runs parallel to the column saturation curve (slightly below since the boundary layer is not saturated). As $\hat{T}$ increases, the onset of conditional instability (assumed in this prototype to yield onset of convective precipitation) occurs at progressively lower free-tropospheric relative humidity, resulting in a curve that angles away from the saturation boundary. This effect depends on the vertical profile associated with the temperature increases and on the effects of entrainment of moist versus drier air in the lower free troposphere. Essentially, in the model and in prior work with the reanalysis (SNHN12), the temperature increases sampled within the current climate tend to be

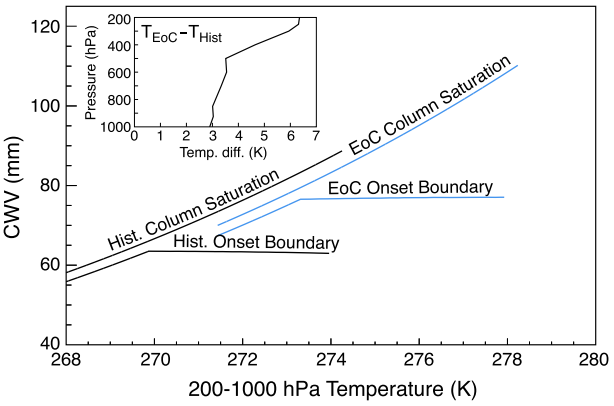

FIG. 8. Precipitation onset boundary, similar to that shown in Figs. 1c and 5, but for a simplified prototype using idealized perturbations to Nauru profiles. Contours of 100 J kg^{-1} entraining CAPE computed by a one-dimensional entraining plume model, or free-tropospheric saturation (seen at lower $\hat{T}$ values, see text), are shown as a measure of the onset boundary of precipitation (by conditional instability or large-scale saturation) for the historical and EoC. The model and the procedure are similar to that discussed in SNHN12. For the historical computations, vertically constant temperature perturbations of 0.2 K are applied to the Nauru mean state conditioned on high values of CWV representative of deep convective cases, whereas for the EoC, similar perturbations are applied to the conditioned temperature profile shifted by the CCSM4 temperature anomaly profile over Nauru for the EoC (shown in the inset). The corresponding column saturation curves are shown for comparison.

associated with temperature profiles modestly more conducive to conditional instability, and thus the entraining parcel is buoyant at slightly lower values of environmental relative humidity. For the sake of simplicity and graphical clarity, the case shown here uses a vertically constant increment of temperature relative to a reference profile. This slightly exaggerates the angle of the onset boundary relative to saturation, with the onset boundary almost constant in CWV. Changing the temperature profile to increase slightly with height or increasing the entrainment causes this boundary to angle upward as a function of $\hat{T}$ (see SNHN12 for examples, including reanalysis temperature profile changes and the precise parcel computation from the CCSM convective scheme). The appendix elaborates on this in more detail.

With this as our prototype for the observed and modeled precipitation onset in the historical case, we can now create a simple prototype for the changes under global warming. For the EoC computations, the CCSM4 temperature profile anomaly (EoC − Hist.) over Nauru (shown as an inset in Fig. 8) is added to the observed base temperature profile used for the historical case. This warmer profile is then used as a base profile to which the same set of temperature and free-tropospheric relative humidity perturbations are added, as in the historical case.

In other words, we assume that the natural variations in the warmer climate sample a similar set of perturbation temperature and free-tropospheric relative humidity profiles as in the historical climate, but all are shifted by the average temperature profile anomaly that the model simulates for the global warming case relative to the historical period. The onset boundary for EoC in Fig. 8 exhibits features much like the historical case. The lower-$\hat{T}$ segment of the curve is governed by saturation, and the higher $\hat{T}$ segment by conditional instability with a very similar angle to column saturation, as seen in the historical case (the column saturation curve for EoC is not quite the same as that for the historical, because the vertical structure of the temperature differs slightly).

The entire structure of the onset boundary at EoC shifts to higher values of CWV and $\hat{T}$ in a manner dictated by the global warming temperature anomaly profile in this prototype. This shift does not follow the angle of the historical onset curve in the CWV–$\hat{T}$ plane simply because the global warming temperature anomaly vertical profile is different. The global warming anomaly profile (Fig. 8 inset) increases with height in a manner similar to a moist adiabat (although modified by entrainment and freezing parameterizations), with a shape generally consistent with those noted in other models (Santer et al. 2005). However, the prototype suggests that the onset boundary at EoC can be obtained from that in the historical case by simple conditional instability calculations if one trusts the climatological mean temperature anomaly vertical structure simulated by CCSM for the global warming case. Furthermore, the prototype suggests that the CCSM EoC temperature anomaly has a vertical profile that yields results from the conditional instability calculation that can be reasonably approximated by a constant relative humidity assumption, as outlined in the appendix. The appendix also shows a variant of Fig. 8 that permits the slight departures from constant relative humidity to be seen.

Overall, this provides an economical explanation of the features of the onset boundary seen in CCSM (Fig. 5a) for both historical and EoC cases. In CCSM and observations, the vertical temperature structures sampled in natural variability tend to be slightly more unstable at warmer temperature for a given relative humidity (see also SNHN12). The prototype allows the different effects of the global warming temperature profile to be seen in a very simple context and also explains why a constant relative humidity assumption works as a reasonable approximation for obtaining the EoC onset boundary from the historical boundary (Fig. 5b). These calculations also provide the caveat that the shift under global warming for the conditional instability portion of the precipitation onset boundary depends on trusting the model simulation of the change in the vertical temperature profile under global warming.

5. Discussion

The recent availability of large datasets for snapshots of precipitation-related variables from remote sensing retrievals, or high time resolution data, such as from the Atmospheric Radiation Measurement Program sites, makes it possible to seek statistics, which might be termed fast-process diagnostics, that can help us to understand and constrain the fast-physics processes that play a major role in the global hydrological cycle. Examples of this include sets of related statistics for the onset of tropical precipitation [such as Bretherton et al. (2004); PN06; NPH09; HN09], which can serve as additional evaluation metrics for climate models. Because the statistics often rely on satellite retrievals that can have their own inherent uncertainties, the comparison to models can also provide a consistency check on observations. Using outputs from both uncoupled and coupled versions of the NCAR CCSM, some of the deep convective onset characteristics are analyzed, including pickup of precipitation and probability distributions for precipitating points as a function of column water vapor. After comparing to statistics from satellite retrievals in current climate, we ask how the model-simulated statistics change under global warming.

a. Simulations for current climate

Analysis of model output from an uncoupled version of the NCAR CCSM, run in an AMIP mode at a fairly high spatial resolution of 0.5°, yields a good match to previously reported deep convective transition statistics using observations (PN06; NPH09). The precipitation pickup is similar to the findings of SNHN12, including the simulation of the dependence of the convective onset boundary in a thermodynamic plane of column water vapor and a bulk measure of tropospheric temperature $\hat{T}$. From SNHN12, it is known that this depends on the model's convective parameterization having a reasonable representation of entrainment and that it can be captured by column-conditional instability calculations, either using the exact convective calculation used in the model or related simplifications.

Assessing the probability distributions for precipitating grid points, the model distributions exhibit a Gaussian core just below the critical CWV value, with a longer-than-Gaussian tail that extends above the critical point for the onset of deep convection in agreement with the satellite retrieval datasets. In this regard, the model can be viewed as corroborating the retrieval-based statistics, which, despite validating well against in situ

observations at particular locations (HN09), should be viewed with caution in the high water vapor and precipitation range. As expected, the model exhibits a neat cutoff at column saturation such that the longer-than-Gaussian portion is restricted to a range between the Gaussian core and saturation. Degrading the model temperature observations to a grid comparable to temperature reanalysis affects the distribution tails modestly, suggesting this is a useful step when comparing models to observations, but the basic structure of the core–tail behavior is robust to this. NPH09 had been cautious in interpreting the long tails until subsequent studies showed the widespread existence of comparable tails in reanalyses, model simulations, and retrievals of other tracers (Neelin et al. 2010; Lintner et al. 2011). Simple stochastic models can yield such tails under plausible assumptions (Stechmann and Neelin 2011). Here, the CAM simulation of the longer-than-Gaussian tail range provides evidence that this can be straightforward to simulate in a full atmospheric model for this high CWV, high precipitation regime. Of course, this regime can only be captured if the onset of conditional instability occurs sufficiently below column saturation, so the reasonable simulation of the onset boundary as seen in the CAM is a prerequisite.

The same convective onset statistics for the 20-yr period 1980–99 from the CMIP5 historical run for CCSM4 at 1° resolution are highly comparable to those of the uncoupled atmospheric model outputs at 0.5° resolution. Thus, the fully coupled model statistics agree well with the uncoupled versions of the model, and these are not highly sensitive to resolution. The occurrence probability of precipitating points shows similarly good agreement with observations, including the longer-than-Gaussian tail related to extremes in convection. The core and the tail each exhibit more variation from one tropospheric temperature bin to another in both uncoupled and coupled simulations than in the observational estimates. While this is a next-order effect, it appears to be an important one for questions of global warming, as discussed below.

b. *Changes under global warming*

Because the coupled version of the model shows broad agreement with the observations for the present-day conditions in terms of some of the deep convection statistics analyzed in this study, it is tempting to investigate how these convection-related statistics evolve under a warmer climate. Comparing convective onset statistics from years 2081–2100 of CCSM4 output for the CMIP5 RCP8.5 global warming scenario to the historical case suggests a number of points: (i) The abrupt pickup in rainfall and the corresponding critical value of CWV shift to higher values of moisture as the system shifts to warmer temperatures, as expected. The convective onset curve in the temperature–water vapor plane continues to have a dependence more complex than saturation, since this boundary seems to be set by the onset of conditional instability for deep convection (as shown for the historical period in NPH09 and SNHN12). (ii) The way this onset curve temperature dependence changes under global warming differs from a simple extension of the temperature dependence in the historical period because the vertical structure of the temperature change differs. Taking an idealized column-conditional instability calculation for the historical temperature–moisture dependence and adding the tropical mean temperature change profile associated with global warming provides a simple prototype for the end-of-century onset boundary. The global warming case can be roughly approximated by using column-relative humidity at each bulk temperature to shift the curve from the historical period. However, the column calculation shows that this is only an approximation and underlines the caveat that this would be sensitive to the vertical structure of the temperature change. (iii) The critical value of CWV continues to strongly govern the frequency of occurrence of precipitating points under global warming. To a first approximation, the PDF of precipitating points as a function of CWV for a given temperature remains the same when column water vapor is normalized by the critical value (and each temperature is shifted by the mean increase). However, this normalization allows modest changes in the shape of the PDF to be seen, and these are particularly noticeable at water vapor values above critical. (iv) Specifically, the longer-than-Gaussian tail above critical CWV, which occurs in both observations and model in the historical period, tends to have increased probability in the end-of-century period under global warming in the model. This occurs in the high water vapor regime between the Gaussian core just below critical and a cutoff at saturation. For most temperatures, this above-critical probability increase is seen as a modification of the slope of the longer-than-Gaussian tail (although for the eastern Pacific at the highest temperature, the modification is sufficient to yield a secondary peak in the PDF in the supercritical range). (v) As a result, conditional average precipitation pickup curves and precipitation variance as a function of CWV reach substantially higher values than in historical simulations. Synoptic examination of events in which supercritical CWV values occur suggests that these events are not qualitatively different from those simulated in the historical period. It simply more often occurs that points in the center of the simulated storm-like clusters of convecting grid points reach very high water vapor and associated high precipitation rates under global warming.

One can now ask to what extent the comparison of modeled convective onset statistics to observed estimates in the historical period may permit inference as to the trustworthiness of the model-simulated statistics under global warming. First, we have a reasonable understanding of the way conditional instability sets the critical value for the convective onset boundary in the historical period and evidence that the model does a good job at simulating this for the type of temperature variations encountered within historical climate. This boosts confidence in the model prediction of the way this shifts under global warming (although the conditional instability calculation suggests that this shift could be sensitive to the details of the simulated vertical temperature structure). The shift in the convective onset boundary governs leading-order effects in the shifts of frequency of occurrence.

The clearest differences in CWV distributions for precipitating points at EoC occur in the longer-than-Gaussian tail above critical, and this is associated with excursions above the onset of conditional instability (into the range between onset and saturation) happening more readily in the global warming simulation. Since the distributions are examined with respect to CWV normalized by a critical value that has increased roughly proportional to column saturation, any changes in distribution that would be directly due to saturation changes are already taken into account. This would include not only the shift in the mean of the distribution but any stretching that was simply proportional to the change in saturation. The change in the shape of the distribution tails must thus be associated with more complex effects, such as a dynamical response of the model storm systems. The longer-than-Gaussian tail shows more variation when evaluated as a function of tropospheric temperature in the historical period in the model simulations than in the observational estimates. However, there are sufficient caveats on the combination of microwave retrievals and reanalysis temperatures in the observational estimates in this high water vapor, high precipitation range that this does not necessarily imply lower trust in the model-simulated tails. Rather, the importance of the changes in these tails for the extreme event statistics in the global warming simulation should be taken as motivation for acquiring additional observational data in this range and comparing the behavior of additional models.

Acknowledgments. This work was supported in part by National Science Foundation Grant AGS-1102838, National Oceanic and Atmospheric Administration Grants NA11OAR4310099 and NA14OAR4310274, and Department of Energy Grant DE-SC0006739. We thank J. E. Meyerson for graphical assistance and S. Krueger for discussions and clarifications.

APPENDIX

Interpretations of the CCSM4 Convective Onset Boundary from Idealized Plume Buoyancy Computations

Figure A1 repeats the idealized calculation of section 4, presenting it in terms of relative humidity and then further breaking it down in a way that helps to visualize the role of competing effects associated with the vertical profile of temperature changes in the environment on the conditional instability boundary. Writing the moist static energy of the environment as

$$h = s(T) + Lq, \tag{A1}$$

the effect of the environment on parcel stability has two components associated with environmental temperature T and environmental moisture q, respectively, and these can vary independently. Temperature of course directly affects the environmental dry static energy

$$s(T) = cpT + \phi(T), \quad \text{with} \quad \phi(T) = \int_{p}^{p_s} RT(p')\, dlnp', \tag{A2}$$

where $\phi(T)$ is the geopotential. Environmental temperature also affects the specific humidity of environmental air that is entrained, when considering a given relative humidity. We can express the temperature–moisture plane in terms of relative humidity in the free troposphere: that is, q in Eq. (A1) is expressed as

$$q = rq_{\text{sat}}(T), \tag{A3}$$

where r is the relative humidity. In the idealized calculation, r is taken as constant for pressures less than 800 mb, transitioning to a specified value at 1000 mb, as described in section 4.

For a nonentraining plume, rising from specified temperature and relative humidity at 1000 mb, the buoyancy at any given level in the free troposphere would only be affected by the temperature profile of the environment relative to the moist adiabat specified by the 1000 mb values. The value of q or r above the starting level would be irrelevant to the buoyancy. In contrast, an entraining plume is also affected by the moisture of the environment, as different values of environmental h are mixed into the parcel during ascent. As a result, higher moisture tends to yield greater conditional instability for a given temperature profile and entrainment rate. When the temperature

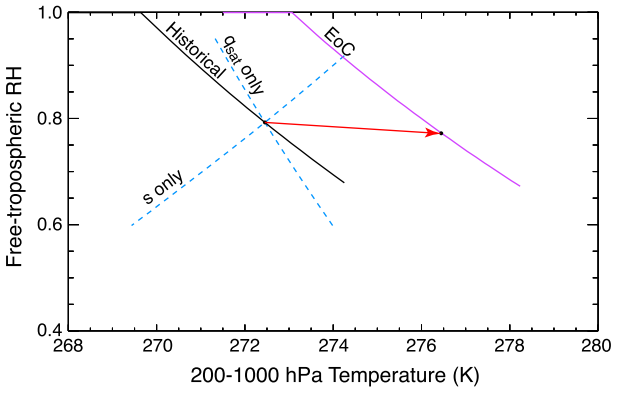

FIG. A1. Simplified prototype for the onset boundary for the present day (solid black curve marked historical) and global warming (solid purple curve marked EoC). These curves correspond to Fig. 8, except that the moisture axis is given in terms of free-tropospheric relative humidity. The red arrow indicates shift associated with global warming temperature change profile. Temperature changes along the historical and EoC curves have a different vertical profile (as in Fig. 8). Dashed lines for the historical case show calculations that examine the effects of temperature via dry static energy s and q_{sat} in the conditional instability calculation that defines the onset boundary.

profile is changed slightly, the relative humidity needed to achieve the onset of conditional instability for an entraining plume changes accordingly, and the idealized calculations aim to develop intuition for this.

For certain changes in temperature profile, the onset of conditional instability occurs at lower relative humidity for higher temperatures, as occurs when sampling temperatures in present-day observations (Fig. 1c), or for similar sampling of the model in both present-day and end-of-century conditions (Fig. 5a). In the idealized calculation, this is illustrated by adding vertically constant temperature perturbations to the base-state profile, which is more destabilizing in terms of the change of the temperature profile than either perturbations of a moist adiabat or the temperature change associated with global warming in CCSM. Increasing temperature would yield increased conditional instability unless r decreases, so the curve of constant entraining CAPE that marks the stability boundary must slope toward lower r with higher T (black solid curve in Fig. A1).

If the temperature change has a different vertical profile, the net effect of the respective tendencies due to the temperature profile and to r can be different. In particular, if the temperature increases sufficiently with height, as occurs for the global warming temperature change profile, then the effect is closer to neutral in terms of requiring little change in r to achieve the onset of conditional instability. In Fig. A1, the shift associated with adding the global warming temperature change profile to the base profile is indicated by the red arrow. The slope of this line is still slightly negative (i.e., to obtain the same value of entraining CAPE, r must decrease slightly). However, this decrease is small enough that one could plausibly consider using a constant relative humidity approximation, with suitable caveats. In particular, modest differences in the vertical profile of the global warming temperature change could affect this significantly.

Within the warmer climate, the convective onset boundary simulated in CCSM has similar slope to that in the historical period (Fig. 5), but the entire onset structure is shifted. In the idealized calculation, the global warming case uses a new base-state profile [i.e., the historical base state plus global warming change profile from CCSM (black dot on the EoC curve in Fig. A1)]. Variations about this within the warmer climate are represented by again using the vertically constant profile added to the new base-state profile, as described in section 4. This results in a curve (purple curve in Fig. A1) with similar slope in the r–$\hat{T}$ plane to that seen in the historical period but shifted by an amount given by the global warming temperature change. This shift (red arrow in Fig. A1) is at a different angle in the r–$\hat{T}$ plane because the global warming temperature structure from the model is less destabilizing (for a given r) than the temperature structure typifying the variations sampled within a given climate. The shift puts the point for the new base state at just slightly lower free-tropospheric relative humidity than the corresponding point on the current climate onset boundary. The idealized historical and EoC curves continue along $r = 1$ for the part of the diagram in which conditional instability of entraining plume does not occur for $r < 1$ because the onset of precipitation would instead occur by large-scale saturation. Note that these features of Fig. A1 correspond exactly to those in Fig. 8 described in section 4 but with the moisture axis given in terms of r.

To further develop intuition regarding the impacts of different effects of the environmental profile on the stability boundary for entraining plumes, consider two additional idealized calculations for the historical case (dashed blue lines in Fig. A1). It is of interest to distinguish between 1) the direct effects of the environmental temperature profile on stability, largely via the comparison between the environmental temperature and that of the entraining parcel lifted from 1000 mbar, and 2) the effects that occur via q_{sat} in Eq. (A1) and Eq. (A3), which depend entirely on the impact of the entrained air on the parcel. To visualize the effects associated with the direct effect of temperature on s, this calculation is repeated with no temperature perturbation applied in $q_{sat}(T)$, referred to as the s-only case. Initial parcel properties at 1000 mbar are still as described in section 4. Dry static energy increases then tend to decrease conditional

instability unless r increases, so the s-only case stability boundary must slope toward higher r with higher T. The complementary q_{sat}-only case repeats the idealized calculation with no temperature perturbation applied in any part of the calculation except the environmental q_{sat}. The temperature increases in this case increase environmental moisture and thus the buoyancy of entraining parcels unless r decreases, so the stability boundary must slope toward lower r with higher T. This negative slope is larger in magnitude than the positive slope of the s-only case, indicating that this effect is stronger. As a result, in the full calculation where both temperature effects on s and q_{sat} are included, the stability boundary has negative slope in the free-tropospheric relative humidity–temperature plane. In a CWV–temperature plane, this corresponds to the onset boundary angling away from saturation as a function of temperature, as seen in Fig. 8.

In summary, this idealized conditional instability calculation provides a succinct prototype for the convective onset boundary, as seen in both the current climate and simulated global warming climate and for the shift between these. At a given environmental relative humidity, environmental temperature changes yield competing tendencies between the effects of s and q_{sat} on the stability of an entraining parcel. Slight differences in the profile of temperature change can yield substantial differences in the slope of the convective onset boundary in a temperature–moisture or temperature–relative humidity plane. For the vertical profile of global warming temperature change in CCSM4, the onset boundary for current climate is shifted in a manner that is sufficiently similar to what would be obtained from a constant relative humidity assumption that the latter can be used as reasonable approximation to attain the future onset boundary from the onset boundary in the historical period.

REFERENCES

Allan, R. P., and B. J. Soden, 2008: Atmospheric warming and the amplification of precipitation extremes. *Science,* **321,** 1481–1484, doi:10.1126/science.1160787.

Bourlioux, A., and A. J. Majda, 2002: Elementary models with probability distribution function intermittency for passive scalars with a mean gradient. *Phys. Fluids,* **14,** 881–897, doi:10.1063/1.1430736.

Bretherton, C. S., M. E. Peters, and L. E. Back, 2004: Relationships between water vapor path and precipitation over the tropical oceans. *J. Climate,* **17,** 1517–1528, doi:10.1175/1520-0442(2004)017<1517:RBWVPA>2.0.CO;2.

Brown, R. G., and C. Zhang, 1997: Variability of midtropospheric moisture and its effect on cloud-top height distribution during TOGA COARE. *J. Atmos. Sci.,* **54,** 2760–2774, doi:10.1175/1520-0469(1997)054<2760:VOMMAI>2.0.CO;2.

Chen, M., R. E. Dickinson, X. Zeng, and A. N. Hahmann, 1996: Comparison of precipitation observed over the continental United States to that simulated by a climate model. *J. Climate,* **9,** 2223–2249, doi:10.1175/1520-0442(1996)009<2233:COPOOT>2.0.CO;2.

Chou, C., and J. D. Neelin, 2004: Mechanisms of global warming impacts on regional tropical precipitation. *J. Climate,* **17,** 2688–2701, doi:10.1175/1520-0442(2004)017<2688:MOGWIO>2.0.CO;2.

——, ——, C.-A. Chen, and J.-Y. Tu, 2009: Evaluating the ''rich-get-richer'' mechanism in tropical precipitation change under global warming. *J. Climate,* **22,** 1982–2005, doi:10.1175/2008JCLI2471.1.

——, C.-A. Chen, P.-H. Tan, and K. T. Chen, 2012: Mechanisms for global warming impacts on precipitation frequency and intensity. *J. Climate,* **25,** 3291–3306, doi:10.1175/JCLI-D-11-00239.1.

——, T.-C. Wu, and P.-H. Tan, 2013: Changes in gross moist stability in the tropics under global warming. *Climate Dyn.,* **41,** 2481–2496, doi:10.1007/s00382-013-1703-2.

Covey, C., K. M. AchutaRao, U. Cubasch, P. Jones, S. J. Lambert, M. E. Mann, T. J. Phillips, and K. E. Taylor, 2003: An overview of results from the Coupled Model Intercomparison Project. *Global Planet. Change,* **37,** 103–133, doi:10.1016/S0921-8181(02)00193-5.

Dai, A., 2006: Precipitation characteristics in eighteen coupled climate models. *J. Climate,* **19,** 4605–4630, doi:10.1175/JCLI3884.1.

——, and K. E. Trenberth, 2004: The diurnal cycle and its depiction in the Community Climate System Model. *J. Climate,* **17,** 930–951, doi:10.1175/1520-0442(2004)017<0930:TDCAID>2.0.CO;2.

——, F. Giorgi, and K. E. Trenberth, 1999: Observed and model-simulated diurnal cycles of precipitation over the contiguous United States. *J. Geophys. Res.,* **104,** 6377–6402, doi:10.1029/98JD02720.

Del Genio, A. D., and J. Wu, 2010: The role of entrainment in the diurnal cycle of continental convection. *J. Climate,* **23,** 2722–2738, doi:10.1175/2009JCLI3340.1.

Held, I. M., and B. J. Soden, 2006: Robust responses of the hydrological cycle to global warming. *J. Climate,* **19,** 5686–5699, doi:10.1175/JCLI3990.1.

Hilburn, K. A., and F. J. Wentz, 2008: Intercalibrated passive microwave rain products from the Unified Microwave Ocean Retrieval Algorithm (UMORA). *J. Appl. Meteor. Climatol.,* **47,** 778–794, doi:10.1175/2007JAMC1635.1.

Holloway, C. E., and J. D. Neelin, 2009: Moisture vertical structure, column water vapor, and tropical deep convection. *J. Atmos. Sci.,* **66,** 1665–1683, doi:10.1175/2008JAS2806.1.

Kuang, Z., and C. S. Bretherton, 2006: A mass-flux scheme view of a high-resolution simulation of a transition from shallow to deep cumulus convection. *J. Atmos. Sci.,* **63,** 1895–1909, doi:10.1175/JAS3723.1.

Kummerow, C., and Coauthors, 2000: The status of the Tropical Rainfall Measuring Mission (TRMM) after two years in orbit. *J. Appl. Meteor.,* **39,** 1965–1982, doi:10.1175/1520-0450(2001)040<1965:TSOTTR>2.0.CO;2.

Lintner, B. R., C. E. Holloway, and J. D. Neelin, 2011: Column water vapor statistics and their relationship to deep convection and vertical horizontal circulation, and moisture structure at Nauru. *J. Climate,* **24,** 5454–5466, doi:10.1175/JCLI-D-10-05015.1.

Majda, A. J., and B. Gershgorin, 2013: Elementary models for turbulent diffusion with complex physical features: Eddy diffusivity, spectrum and intermittency. *Philos. Trans. Roy. Soc. London,* **A371,** 20120184, doi:10.1098/rsta.2012.0184.

Mather, J. H., T. P. Ackerman, W. E. Clements, F. J. Barnes, M. D. Ivey, L. D. Hatfield, and R. M. Reynolds, 1998: An atmospheric radiation and cloud station in the tropical western Pacific. *Bull. Amer. Meteor. Soc.,* **79,** 627–642, doi:10.1175/1520-0477(1998)079<0627:AARACS>2.0.CO;2.

Meehl, G. A., C. Covey, B. McAvaney, M. Latif, and R. J. Stouffer, 2005: Overview of the Coupled Model Intercomparison Project. *Bull. Amer. Meteor. Soc.,* **86,** 89–93, doi:10.1175/BAMS-86-1-89.

Muller, C. J., L. E. Back, P. A. O'Gorman, and K. A. Emanuel, 2009: A model for the relationship between tropical precipitation and column water vapor. *Geophys. Res. Lett.,* **36,** L16804, doi:10.1029/2009GL039667.

——, P. A. O'Gorman, and L. E. Back, 2011: Intensification of precipitation extremes with warming in a cloud-resolving model. *J. Climate,* **24,** 2784–2800, doi:10.1175/2011JCLI3876.1.

Neale, R. B., J. H. Richter, and M. Jochum, 2008: The impact of convection on ENSO: From a delayed oscillator to a series of events. *J. Climate,* **21,** 5904–5924, doi:10.1175/2008JCLI2244.1.

Neelin, J. D., O. Peters, J. W.-B. Lin, K. Hales, and C. E. Holloway, 2008: Rethinking convective quasi-equilibrium: Observational constraints for stochastic convective schemes in climate models. *Philos. Trans. Roy. Soc. London,* **A366,** 2579–2602, doi:10.1098/rsta.2008.0056.

——, ——, and K. Hales, 2009: The transition to strong convection. *J. Atmos. Sci.,* **66,** 2367–2384, doi:10.1175/2009JAS2962.1.

——, B. R. Lintner, B. Tian, Q. Li, L. Zhang, P. K. Patra, M. T. Chahine, and S. N. Stechmann, 2010: Long tails in deep columns of natural and anthropogenic tropospheric tracers. *Geophys. Res. Lett.,* **37,** L05804, doi:10.1029/2009GL041726.

O'Gorman, P. A., 2012: Sensitivity of tropical precipitation extremes to climate change. *Nat. Geosci.,* **5,** 697–700, doi:10.1038/ngeo1568.

——, and T. Schneider, 2009: The physical basis for increases in precipitation extremes in simulations of 21st-century climate change. *Proc. Natl. Acad. Sci. USA,* **106,** 14 773–14 777, doi:10.1073/pnas.0907610106.

Osborn, T. J., and M. Hulme, 1998: Evaluation of the European daily precipitation characteristics from the atmospheric model intercomparison project. *Int. J. Climatol.,* **18,** 505–522, doi:10.1002/(SICI)1097-0088(199804)18:5<505::AID-JOC263>3.0.CO;2-7.

Peters, O., and J. D. Neelin, 2006: Critical phenomena in atmospheric precipitation. *Nat. Phys.,* **2,** 393–396, doi:10.1038/nphys314.

Pierrehumbert, R. T., 2000: Lattice models of advection–diffusion. *Chaos,* **10,** 61–74, doi:10.1063/1.166476.

Romps, D. M., 2011: Response of tropical precipitation to global warming. *J. Atmos. Sci.,* **68,** 123–138, doi:10.1175/2010JAS3542.1.

Sahany, S., J. D. Neelin, K. Hales, and R. B. Neale, 2012: Temperature–moisture dependence of the deep convective transition as a constraint on entrainment in climate models. *J. Atmos. Sci.,* **69,** 1340–1358, doi:10.1175/JAS-D-11-0164.1.

Santer, B. D., and Coauthors, 2005: Amplification of surface temperature trends and variability in the tropical atmosphere. *Science,* **309,** 1551–1556, doi:10.1126/science.1114867.

Seo, E. K., B.-J. Sohn, and G. Liu, 2007: How TRMM precipitation radar and microwave imager retrieved rain rates differ. *Geophys. Res. Lett.,* **34,** L24803, doi:10.1029/2007GL032331.

Soden, B. J., D. L. Jackson, V. Ramaswamy, M. D. Schwarzkopf, and X. Huang, 2005: The radiative signature of upper tropospheric moistening. *Science,* **310,** 841–844, doi:10.1126/science.1115602.

Stechmann, S., and J. D. Neelin, 2011: A stochastic model for the transition to strong convection. *J. Atmos. Sci.,* **68,** 2955–2970, doi:10.1175/JAS-D-11-028.1.

——, and ——, 2014: First-passage-time prototypes for precipitation statistics. *J. Atmos. Sci.,* **71,** 3269–3291, doi:10.1175/JAS-D-13-0268.1.

Stokes, G. M., and S. E. Schwartz, 1994: The Atmospheric Radiation Measurement (ARM) Program: Programmatic background and design of the cloud and radiation test bed. *Bull. Amer. Meteor. Soc.,* **75,** 1201–1221, doi:10.1175/1520-0477(1994)075<1201:TARMPP>2.0.CO;2.

Sun, Y., S. Solomon, A. Dai, and R. Portmann, 2006: How often does it rain? *J. Climate,* **19,** 916–934, doi:10.1175/JCLI3672.1.

——, ——, ——, and R. W. Portmann, 2007: How often will it rain? *J. Climate,* **20,** 4801–4818, doi:10.1175/JCLI4263.1.

Trenberth, K. E., A. Dai, R. M. Rasmussen, and D. B. Parsons, 2003: The changing character of precipitation. *Bull. Amer. Meteor. Soc.,* **84,** 1205–1217, doi:10.1175/BAMS-84-9-1205.

——, J. Fasullo, and L. Smith, 2005: Trends and variability in column-integrated atmospheric water vapor. *Climate Dyn.,* **24,** 741–758, doi:10.1007/s00382-005-0017-4.

Uppala, S. M., and Coauthors, 2005: The ERA-40 Re-Analysis. *Quart. J. Roy. Meteor. Soc.,* **131,** 2961–3012, doi:10.1256/qj.04.176.

Wentz, F. J., and R. W. Spencer, 1998: SSM/I rain retrievals within a unified all-weather ocean algorithm. *J. Atmos. Sci.,* **55,** 1613–1627, doi:10.1175/1520-0469(1998)055<1613:SIRRWA>2.0.CO;2.